

# Prior2Former - Evidential Modeling of Mask Transformers for Assumption-Free Open-World Panoptic Segmentation

Sebastian Schmidt<sup>1,2,\*</sup>

Julius Körner<sup>1,2,\*</sup>

Dominik Fuchsgruber<sup>1</sup>

Stefano Gasperini<sup>1,3</sup>

Federico Tombari<sup>1,4</sup>

Stephan Günnemann<sup>1</sup>

<sup>1</sup> Technical University of Munich

<sup>2</sup> BMW Group

<sup>3</sup> Visualais

<sup>4</sup> Google Zurich

## Abstract

In panoptic segmentation, individual instances must be separated within semantic classes. As state-of-the-art methods rely on a pre-defined set of classes, they struggle with novel categories and out-of-distribution (OOD) data. This is particularly problematic in safety-critical applications, such as autonomous driving, where reliability in unseen scenarios is essential. We address the gap between outstanding benchmark performance and reliability by proposing Prior2Former (P2F), the first approach for segmentation vision transformers rooted in evidential learning. P2F extends the mask vision transformer architecture by incorporating a Beta prior for computing model uncertainty in pixel-wise binary mask assignments. This design enables high-quality uncertainty estimation that effectively detects novel and OOD objects enabling state-of-the-art anomaly instance segmentation and open-world panoptic segmentation. Unlike most segmentation models addressing unknown classes, P2F operates without access to OOD data samples or contrastive training on void (i.e., unlabeled) classes, making it highly applicable in real-world scenarios where such prior information is unavailable. Additionally, P2F can be flexibly applied to anomaly instance and panoptic segmentation. Through comprehensive experiments on the Cityscapes, COCO, SegmentMelfYouCan, and OoDIS datasets, we demonstrate the state-of-the-art performance of P2F. It achieves the highest ranking in the OoDIS anomaly instance benchmark among methods not using OOD data in any way.

## 1. Introduction

Semantic understanding is essential for any autonomous agent navigating in the environment or interacting with it. State-of-the-art methods rely on comprehensive datasets

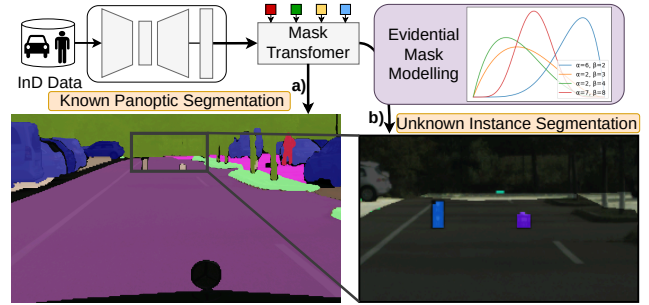


Figure 1. The proposed Prior2Former allows **a)** state-of-the-art panoptic segmentation performance and **b)** identifies unknown instances by uncertainty-based evidential learning without any knowledge beyond the in-domain (InD) training data.

that cover a data distribution of interest [10, 12] but cannot operate beyond that, limiting their applicability in real-world settings where unknown scenarios are the norm [20]. In safety-critical applications, such as mobile robotics or autonomous driving, safe operation in environments outside the training data distribution is crucial [52]. For example, an autonomous car must detect objects on the street regardless of whether their semantic class belongs to the training set and adapt its trajectory accordingly. Consequently, *open-world* segmentation [28] and *anomaly* segmentation [44] recently emerged to study these OOD settings systematically.

Existing methods often approach this problem with powerful external models familiar with such OOD data [42] or through exposure during training to OOD data [28] or *void* categories (i.e., unlabeled) [62]. Some works [42] mitigate this problem by leveraging powerful external models such as CLIP [45]. Often used as black boxes, these external models can be large foundation models with extensive vocabularies that enable the wrapping methods to significantly expand the pool of objects they can handle [42]. However, they assume that these vocabularies encompass every possible object, which is unrealistic, so they fail whenever the input lies outside the vocabulary.

As a dense task, segmentation requires a prediction for every point or pixel of the input. Some datasets annotate pixels not containing relevant elements as *void* [14]. Prior works utilize this by learning the *void* class and associating

\* Equal Contribution

Corresponding author sebastian95.schmidt@tum.de

unknown classes to it during inference [28, 55, 62]. However, they assume that training data’s *void* class is diverse enough to represent unknowns, which is often unrealistic, limiting their ability to handle OOD data [28]. Other approaches model the generative process of unknowns [15].

These works assume knowledge about the distribution of unknown and OOD objects, incorporating known OOD data into the training distribution. However, real-world diversity is limited in the representations of datasets, restricting their real-world applicability with unseen objects (i.e., OOD) significantly [20], in contrast to their exceptional benchmark performance [43]. In contrast, U3HS [20] segments completely unseen, unknown objects without relying on external knowledge or assumptions, but it compromises performance for known classes, creating a trade-off between known and unknown capabilities.

In this paper, we overcome these issues by proposing P2F (Fig. 1), the first vision transformer for segmentation rooted in evidential learning. It combines the Mask2Former (M2F) architecture [12] with prior networks [39] to provide reliable uncertainty estimates that enable the segmentation of unseen objects without compromising performance.

In particular, we explicitly model pixel-wise prior distributions for each binary segmentation mask query in the mask transformer architecture. The concentration parameters of this distribution, the so-called *evidence*, indicate the model’s confidence and inversely correlate to its uncertainty. By learning Bayesian updates to these prior distributions, P2F is highly effective in various open-world applications. Notably, it does *neither require any exposure to OOD data nor any other assumptions* about the unknown classes while maintaining strong performance on known classes. We summarize our main contributions as follows:

- We introduce P2F, the *first* evidential mask transformer that *does not require OOD data or knowledge* and quantifies uncertainty with negligible computational overhead.
- We introduce a novel loss function for training this architecture and improve existing training procedures by evidential sampling.
- We show that P2F achieves state-of-the-art performance among models that do not rely on OOD across the tasks of anomaly segmentation, open-world semantic and panoptic segmentation, and anomaly instance segmentation.

## 2. Related Work

**Closed-World Segmentation:** While early semantic segmentation models employ encoder-decoder CNN architectures [8, 9, 47], recently, transformer-based models [11, 12, 61] have leveraged attention to enhance performance. Panoptic segmentation [31] extends semantic segmentation by categorizing classes into “*stuff*” (amorphous regions) and “*things*” (countable objects), distinguishing also individual instances within semantic “*thing*” classes. Methods

such as Panoptic-DeepLab [10] provide a proposal-free approach to identify the different instances, while the masked approach of Maskformer [11] or M2F [12] directly uses masks to predict instances. They leverage attention to query and assign masks to classes, predicting both instances and semantic stuff classes with the same architecture.

**Uncertainty Estimation:** Uncertainty estimation [21] is important in various domains including active learning [40, 49, 50, 53] or OOD detection [51, 60] and particularly in safety-critical applications like autonomous driving [19]. Approximate Bayesian [18] and ensemble [33] methods offer high-quality estimates but come at a high computational cost as they require multiple forward passes at inference time. Single-pass deterministic approaches instead estimate uncertainty in a sampling-free manner: SNGP [36] uses spectral normalized Gaussian processes, while DDU [40] fits a Gaussian Mixture Model (GMM) based uncertainty estimation of DUQ [2]. SegGMM [34] directly incorporates a GMM into the training process. Prior networks [39, 54] rely on evidential learning and learn a conjugate prior to the predictive distribution from which uncertainty can be estimated. Posterior networks [6, 7, 56] extend this concept by learning Bayesian updates to this conjugate prior from a flow-based data density estimator. Our work builds on this principle by computing a conjugate prior for each pixel in each of the masks of the M2F architecture.

**Open-set and Anomaly Segmentation:** Compared to closed-set, standard segmentation where only a pre-defined set of object categories are considered, in open-world settings, models encounter unknown and novel object categories that are not part of the training data [20, 28, 51]. Open-set segmentation [28] aims to pixel-wise classify known classes while identifying unknown classes, contrasting anomaly segmentation [44] only binary distinguishes known objects from unknown objects, also called anomalies. Benchmarks for anomaly segmentation include Lost & Found (L&F) [44], Fishyscapes (FS) [3], and Segment-MeIfYouCan (SMIYC) [5]. Recent advancements combine the open-world concept with the individual instance segmentation concept and propose open-set panoptic [28] and holistic segmentation [20] as well as anomaly instance segmentation [43] for the binary case.

Open-set and anomaly segmentation approaches can be roughly categorized into three groups: 1) using additional models, 2) relying on additional data and therefore making assumptions about OOD data, and 3) models without additional requirements. While, in the realm of OOD detection for classification, the use of OOD data is explicitly prohibited [63, 65] to ensure generalization, in anomaly segmentation the usage of OOD data or external models is less strict.

1) Approaches using external foundation models can leverage their knowledge from vast datasets with numerous classes. For example, UGAIN [42] uses SAM [32] for

instance-level anomaly segmentation. This paradigm implicitly relies on the foundation model to cover all potential anomaly types even though this is, in practice, unrealistic as objects unknown to the larger model would still exist.

2) Most approaches for anomaly segmentation employ OOD data or *void* regions that contain misc elements that do not belong to any of the other labeled semantic classes. OOD data is used by directly training the model to assign these instances to the void class and an additional OOD class [13, 37, 58]. Maskanomaly [1] and RbA [41] propose mask rejection after tuning on OOD data. Mask2Anomaly [46] aims to learn an additional background mask from OOD samples. EAM [22] generates OOD artifacts through patch cutting during training, while Uno [15] generates synthetic OOD data with a normalizing flow. The use of real and synthetic OOD data during training introduces a distributional prior knowledge about the anomalies that helps the model detect them. ContMav [55] employs contrastive and objectosphere losses to *void* regions for anomaly and open-world segmentation. EOPSN [28] and DDOSP [62] re-identify unlabeled unknown categories that are within the training data’s *void* regions. These methods relying on OOD data or *void* regions perform well on existing benchmarks. However, these benchmarks often satisfy the distribution assumptions that these works rely on [28]. This makes them particularly weak in scenarios where the OOD data comes from different distributions. Therefore, *in line with the holistic segmentation [20] setting, we consider any use of (pseudo-) OOD data, including post-training heuristics, external foundation models, or contrastive learning on void regions, to violate the open-set paradigm as knowledge about OOD categories is leaked into the model.*

3) Only a few approaches are assumption-free in that regard. SML [29] achieves good unknown segmentation performance using standardized logits, while MSP [26] leverages softmax scores directly. U3HS [20] employs a Dirichlet Prior Network based on DeeplabV3+ and clustering of uncertain embeddings to segment and distinguish unknown instances.

*In this work, we develop an uncertainty-aware transformer architecture that does not rely on assumptions about OOD data through evidential learning. While this paradigm has shown potential in previous segmentation models [11, 12, 20, 61], it remains unexplored for transformer-based segmentation. Unlike prior works, this enables our models to segment any type of unknown object while performing strongly on known categories.*

### 3. Preliminaries

We consider a dataset of RGB images  $X \in \mathbb{R}^{H \times W \times 3}$  and panoptic labels  $Y \in \mathbb{N}^{H \times W \times C}$ .

**Mask-Based Prediction:** In contrast to classical architectures, which predict class logits for each pixel indepen-

dently, mask-based architectures [11, 12] generate binary pixel-wise masks, which are then each classified into the  $C$  segmentation labels. First, a backbone extracts image features from which a pixel decoder computes per-pixel embeddings  $F_E \in \mathbb{R}^{E \times H \times W}$ . A transformer then uses masked attention to compute embeddings  $F_M \in \mathbb{R}^{E \times N_M}$  for all  $N_M$  masks and unnormalized per-mask class assignments  $\tilde{P}_M \in \mathbb{R}^{N_M \times C}$ . The similarity between each pixel’s embedding and the mask embeddings determines its (unnormalized) mask correspondence  $\tilde{M} = F_M \cdot F_E \in \mathbb{R}^{H \times W \times N_M}$ . The per-mask class assignments are subject to normalization with the softmax function  $P_M = \sigma_{\text{SM}}(\tilde{P}_M)$  while the per-pixel mask correspondences are normalized with a sigmoid  $M = \sigma(\tilde{M})$ . Finally, the per-pixel segmentation logits are obtained by aggregating the per-mask class assignment for each pixel individually through weighting by its correspondence to each respective mask:

$$L(x)[h, w, c] = \sum_{i=1}^{N_M} P(x)[i, c] \cdot M(x)[h, w, i]. \quad (1)$$

The loss is calculated using mask class assignments and per-pixel correspondences. Labels are represented as  $l_X$  binary masks  $Y_M \in \{0, 1\}^{H \times W \times l_X}$ , which correspond to class labels for each mask  $Y_C \in \{1, \dots, C\}^{l_X}$ . The masks  $M(x)$  are matched to the best-fitting ground-truth mask in  $Y_M$  using a Hungarian matcher. The pixel-to-mask correspondence is trained using a binary cross-entropy  $\mathcal{L}_{\text{BCE}}$  and a dice loss  $\mathcal{L}_{\text{Dice}}$  [57] between  $M(x)$  and  $Y_M$ . Similarly, the per-mask class assignments are trained with a cross-entropy loss  $\mathcal{L}_{\text{CE}}$  between  $P(x)$  and  $Y_C$ . For panoptic segmentation, the label set  $Y$  consists of one binary mask for every stuff class and for each instance per image. Following M2F [12], the loss is computed only for a subset of pixels  $\mathcal{P}$ . Masks in  $M(x)$  not matching any mask in  $Y_M$  are ignored in the mask loss, and the mask classification loss is adjusted to assign them to an additional *no-object* class.

**Evidential Learning:** Traditional models for semantic segmentation apply a softmax  $\sigma_{\text{SM}}$  over the class logits predicted for each pixel. Despite the ubiquity of this paradigm, recent work has found shortcomings in accurately representing model uncertainty resulting from a tendency toward overconfidence [23, 25, 30]. A promising alternative is Evidential Learning [54], which is grounded in Dempster-Shafer Theory [16]. Rather than directly modeling a categorical distribution  $p(y | \mathbf{x}) \sim \text{Cat}(\sigma_{\text{SM}}(L(\mathbf{x})))$  for an instance with features  $\mathbf{x}$ , evidential models parametrize its conjugate prior by predicting the *evidence* for each possible class. For a categorical distribution over  $C$  classes, the conjugate prior is a Dirichlet distribution parametrized by  $K$  concentration parameters  $\kappa = (\kappa_1, \kappa_2, \dots, \kappa_C)$ :

$$\text{Dir}(p|\kappa) = \frac{\Gamma(\sum_{k=1}^K \kappa_k)}{\prod_{k=1}^K \Gamma(\kappa_k)} \prod_{k=1}^K p_k^{\kappa_k - 1} \quad (2)$$

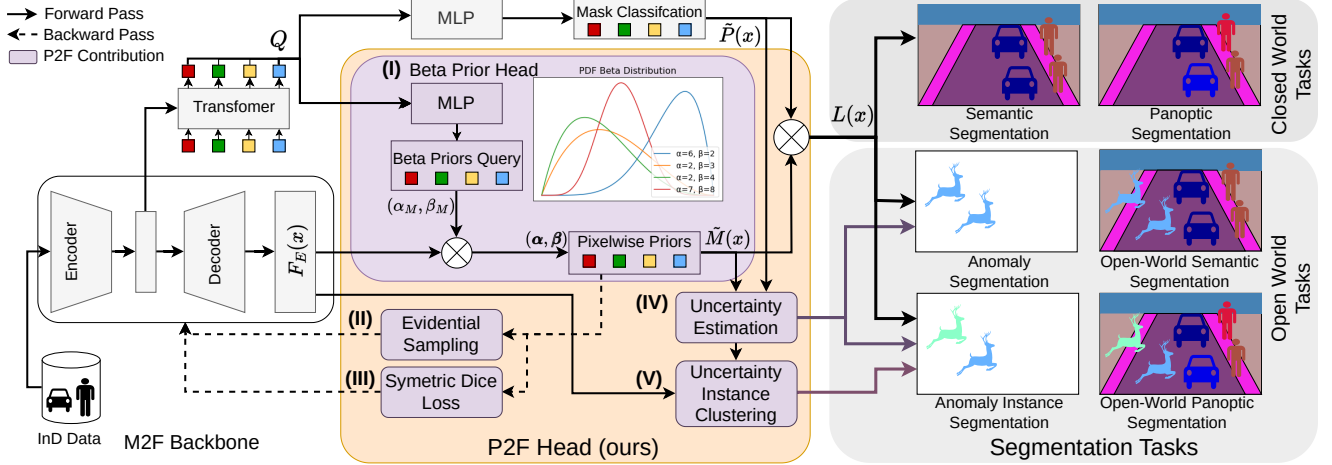


Figure 2. Overview of the Prior2Former architecture composed of a **beta-prior head (I)**, **evidential sampling (II)**, **symmetric dice loss (III)**, **uncertainty estimation (IV)**, and **uncertainty instance clustering (V)**. Only In-distribution data is used to train our Prior2Former (I) using our novel symmetric-dice loss (III) and evidential sampling (III). During inference, our uncertainty estimation (IV) detects anomalous objects, while our uncertainty instance clustering (V) can distinguish the instances of novel classes.

Here,  $\Gamma$  is the gamma function. Intuitively, the (second-order) Dirichlet is a distribution over (first-order) categorical distributions  $p$ . Predicting the conjugate prior to the predictive distribution allows a model to represent different types of uncertainty [48]. Low evidence priors indicate high model uncertainty as the corresponding first-order predictive distributions are less concentrated. Conversely, high evidence priors, which lead to concentrated first-order distributions, correspond to high confidence. This enables the model to predict high-entropy first-order distributions with high confidence to represent data-inherent uncertainty. Notably, first-order distributions alone cannot distinguish between inherent and model-related uncertainty [48], a distinction crucial for downstream anomaly-related applications [40].

## 4. Prior2Former

We propose to leverage the benefits of evidential learning in the context of mask transformers for segmentation to equip them with a way to faithfully represent uncertainty by designing P2F, the first evidential mask transformer architecture. It is trained to predict a second-order prior to its binary per-pixel segmentation masks. This induces uncertainty-aware embeddings that can be used to tackle various closed-world and open-world tasks, including closed-world and open-world panoptic segmentation, anomaly segmentation, and anomaly instance segmentation. All of these tasks can be addressed with the same architecture and training framework *without* requiring additional data or any other assumption about potential anomalies.

P2F predicts the parameters of the conjugate Beta distribution for each segmentation mask through a **beta-prior**

**head (I)** to accurately describe model uncertainty. Additionally, we introduce a novel **evidential uncertainty sampling strategy (II)** and propose a **symmetric dice loss (III)** to train P2F. Both are explicitly tailored toward Beta distributions to increase the quality of the associated mask prediction. Lastly, we convert the predicted mask-based evidence scores into accurate **uncertainty estimates (IV)**. These can be leveraged by an **uncertainty instance clustering (V)** to distinguish between individual anomalous instances. The architecture of P2F is sketched in Fig. 2.

**(I) Beta-Prior Head:** As described in Sec. 3, the conjugate prior in classification problems is a Dirichlet distribution  $\text{Dir}(p|\kappa)$  over all possible categorical distributions. In binary classification, the Beta distribution is used as the conjugate prior to the predictive Bernoulli distribution. It is parameterized by concentration parameters  $\alpha, \beta > 0$ :

$$\text{Beta}(y | \alpha, \beta) = \frac{\Gamma(\alpha + \beta)}{\Gamma(\alpha)\Gamma(\beta)} y^{\alpha-1} (1-y)^{\beta-1}. \quad (3)$$

Here,  $\Gamma$  is the gamma function. The concentration parameters can be interpreted as pseudo-counts for positive and negative observations of the corresponding Bernoulli variable. Their magnitude, therefore, serves as evidence and can be used for uncertainty quantification.

We therefore extend the M2F architecture to not directly predict the (unnormalized) mask assignments  $F_M(x)$  but instead the corresponding concentration parameters  $\alpha_M(x), \beta_M(x) \in \mathbb{R}^{N_M \times E}$ . Similarly to how M2F computes  $\tilde{M}(x)$ , we use multiplication to obtain per-pixel evidences  $\alpha(x), \beta(x) \in \mathbb{R}^{H \times W \times N_M}$ :

$$\alpha(x) = \alpha_M(x) \cdot F_E(x) \quad \beta(x) = \beta_M(x) \cdot F_E(x). \quad (4)$$



While the M2F architecture uses an element-wise sigmoid to compute soft pixel-to-mask assignments as  $M(x) = \sigma(\tilde{M}(x))$ , we propose to instead use the expected first-order pixel-to-mask assignment in P2F:

$$M(x) = \mathbb{E}_{\mathbf{p} \sim \mathbf{B}(\boldsymbol{\alpha}(x), \boldsymbol{\beta}(x))}[\mathbf{p}] = \frac{\boldsymbol{\alpha}(x)}{\boldsymbol{\alpha}(x) + \boldsymbol{\beta}(x)}. \quad (5)$$

For each pixel, the concentration parameters  $\alpha, \beta$  indicate the evidence the model assigns to the positive and negative class respectively. Therefore, they induce an evidence-based uncertainty score:

$$\mathbf{U}_{\text{evi}}(x) = -(\boldsymbol{\alpha}(x) + \boldsymbol{\beta}(x)). \quad (6)$$

Intuitively, for a given pixel and mask, the M2F model assigns high uncertainty only if it does not predict any evidence for either the positive or negative class.

**(II) Evidential Sampling:** During the training P2F predicts concentration parameters of the Beta prior  $\boldsymbol{\alpha}_M, \boldsymbol{\beta}_M$ . We compute them as the similarity scores between the output of a mask query MLP and the pixel-wise representations of the decoder. By first applying a softplus function and then incrementing all values by 1, we satisfy the positivity constraint on the concentration parameters. Consequently, the resulting Beta prior is always non-degenerate, and its expected values – the mask probabilities  $M(x)$  – are always in the open interval  $(0, 1)$ .

We adapt the mask sampling procedure of M2F [12] that is outlined in Sec. 3 and represent the segmentation masks through  $l_X$  binary ground-truth binary targets  $Y_M \in \{0, 1\}^{H \times W \times l_X}$ . In panoptic tasks, we use an individual mask for each instance within the image and each stuff class. Each of the  $N_M$  masks  $i$  predicted by P2F is then matched to a mask  $\hat{i}$  in  $Y_M$ . We refer to masks that were matched as *predicted masks* and index them with  $\mathcal{M}(x) \subseteq \{1, \dots, N_M\}$ . For each mask  $i \in \mathcal{M}(x)$ , only a subset of pixels  $\mathcal{P}_i(x)$  is sampled to calculate the loss with respect to the matched target mask  $\hat{i}$ .

We utilize the evidential uncertainty of P2F to improve the training efficiency through an evidence-based sampling strategy for each mask  $\mathcal{P}_i(x)$ . For a given budget of pixels for which the training loss is to be computed, we assign 75% of it to pixels with the highest evidential uncertainty according to Eq. (6) and randomly select the remaining 25%. This steers the training to focus on regions with high evidential uncertainty. The corresponding loss maximizes the log-likelihood of the ground-truth masks under the predicted Beta prior:

$$\mathcal{L}_{\text{evi}}(Y_M, x) = \frac{1}{|\mathcal{M}(x)|} \quad (7)$$

$$\sum_{i \in \mathcal{M}(x)} \mathcal{L}_{\text{evi}}(Y_M(x)[\dots, \hat{i}], \boldsymbol{\alpha}(x)[\dots, i], \boldsymbol{\beta}(x)[\dots, i]) \quad (8)$$

where  $\mathcal{L}_{\text{evi}}(Y, \boldsymbol{\alpha}, \boldsymbol{\beta}) =$

$$\sum_{h, w \in \mathcal{P}_i(x)} -\log \text{Beta}(Y[h, w] \mid \boldsymbol{\alpha}[h, w], \boldsymbol{\beta}[h, w]). \quad (9)$$

**(III) Symmetric Dice Loss:** The task of predicting binary segmentation masks is highly imbalanced. Therefore, we introduce a novel symmetric dice loss to prevent updates that predominantly focus on  $\beta$ :

$$\begin{aligned} \mathcal{L}_{\text{sDice}}(Y_M, x) = & \frac{1}{2} \left( \mathcal{L}_{\text{Dice}} \left( \frac{\boldsymbol{\alpha}(x)}{\boldsymbol{\alpha}(x) + \boldsymbol{\beta}(x)}, Y_M \right) \right. \\ & \left. + \mathcal{L}_{\text{Dice}} \left( \frac{\boldsymbol{\beta}(x)}{\boldsymbol{\alpha}(x) + \boldsymbol{\beta}(x)}, 1 - Y_M \right) \right). \end{aligned} \quad (10)$$

Here,  $\mathcal{L}_{\text{Dice}}$  refers to the standard dice loss between the predicted probabilities and the true segmentation. The total loss to train P2F combines the evidential and the symmetric dice losses with the cross-entropy loss  $\mathcal{L}_{\text{CE}}$  of Sec. 3:

$$\mathcal{L}_{\text{P2F}} = \lambda_{\text{CE}} \mathcal{L}_{\text{CE}} + \lambda_{\text{sDice}} \mathcal{L}_{\text{sDice}} + \lambda_{\text{evi}} \mathcal{L}_{\text{evi}}. \quad (11)$$

We compute all losses on the same pixel sets  $\mathcal{P}_i$ . In contrast to other approaches, P2F is not explicitly trained to reject anomalous instances by assigning them to an additional *void* class. Therefore, we do not require any form of OOD data or surrogates that (implicitly) make assumptions about its distribution to train P2F.

**(IV) Uncertainty Estimation:** We now outline how the evidence-based mask uncertainty of Eq. (6) can be combined with the mask classification  $P(x)$ . First, we disregard all masks  $\mathcal{M}_\emptyset \subseteq \{1, \dots, N_M\}$  that are classified as *no-object*. For each of the remaining masks, P2F represents its confidence in a pixel being assigned to the mask through the concentration  $\boldsymbol{\alpha}$ . The confidence with which P2F assigns a pixel to any class is therefore represented by the highest evidence over all masks. For the corresponding mask  $i^*$  (Eq. (12a)), we obtain the probability of a pixel being assigned to this mask as the expectation under the predicted Beta prior  $p_M^*$  (Eq. (12b)). We use this probability to re-weight the confidence  $p_C^*$  with which the corresponding mask is classified (Eq. (12c)). Finally, the uncertainty  $U$  associated with the segmentation of a pixel is quantified as inversely correlated with this weighted classification confidence (Eq. (12d)). Effectively, our procedure adjusts the uncertainty arising from mask classification by re-weighting it according to the evidential pixel-wise uncertainty in the predicted mask.

$$i^*(h, w) = \arg \max_{i \in \{1, \dots, N_M\} \setminus \mathcal{M}_\emptyset} \boldsymbol{\alpha}(x)[h, w, i] \quad (12a)$$

$$p_M^*(h, w) = \left( \frac{\boldsymbol{\alpha}(x)}{\boldsymbol{\alpha}(x) + \boldsymbol{\beta}(x)} \right) [h, w, i^*(h, w)] \quad (12b)$$

$$p_C^*(h, w) = \max_c \sigma_{\text{SM}}(\tilde{P}_M(x)[i^*(h, w), c]) \quad (12c)$$

$$U(h, w) = -p_C^*(h, w) \cdot p_M^*(h, w) \quad (12d)$$

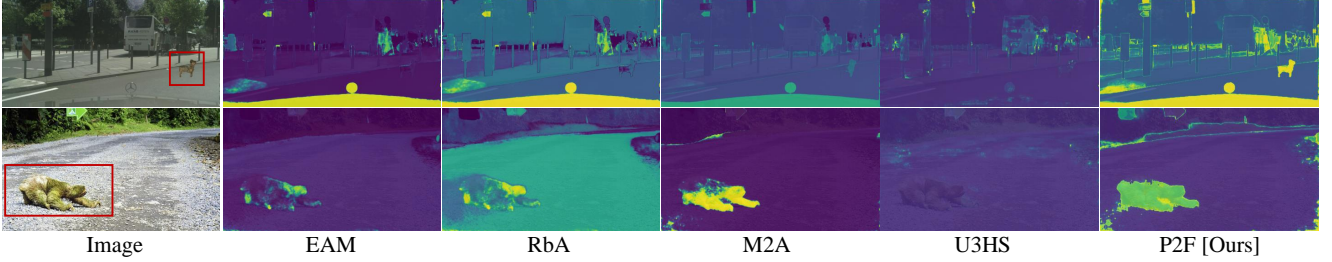


Figure 3. Visual comparison of different uncertainty estimates for binary anomaly segmentation task on FS [3] (top) and SMIYC Road Anomaly [5] (bottom).

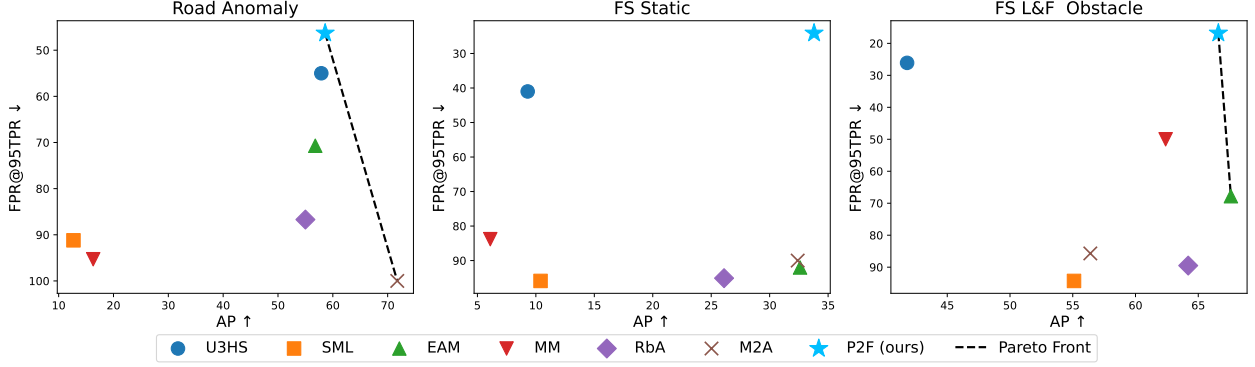


Figure 4. Anomaly Segmentation Benchmarks using the official SMIYC benchmark code on the validation sets for SMIYC Road Anomaly, FS Static, and the FS L&F obstacle track. P2F shows the best trade-off between AP and FPS for all three benchmarks.

**(V) Uncertainty Instance Clustering:** To distinguish between different uncertain instances, we utilize the embeddings from the pixel decoder  $F_E$  and our uncertainty  $U$  from Eq. (12). By thresholding the uncertainty scores Eq. (12), we obtain candidates for anomaly segmentation. The corresponding pixel embeddings from the pixel decoder  $F_E$  are then clustered using DBScan [17]. Details on the threshold are given in Appendix A. The pixels that are not assigned to any cluster are reassigned to the original semantic class and instance respectively. In contrast to U3HS [20] which also employs clustering-based anomaly instance segmentation, P2F further streamlines the model, avoiding contrastive training losses.

## 5. Experiments

We comprehensively evaluate P2F across various tasks and settings. Our primary focus encompasses four tasks: **anomaly segmentation** and **anomaly instance segmentation** as well as **open-world semantic** and **panoptic segmentation**. To underline the ability of P2F to address *all* tasks with the *same* architecture and training strategy, we adopt a panoptic training strategy outlined in Sec. 3 for all experiments. Details regarding the experimental settings are provided in Appendix A.

**Anomaly Segmentation:** First, we study the anomaly segmentation capabilities of P2F by comparing ours with

state-of-the-art anomaly segmentation approaches. In this binary segmentation task, anomalous objects must be identified. We employ the existing benchmarks L&F [44], FS [3], and SMIYC [5]. To maintain a fair comparison, we implement all models with the same ResNet50 [24] backbone and train with the same panoptic training procedure without utilizing OOD data. We use the official SMIYC benchmark code to report the Average Precision (AP) and False Positive Rate (FPR) for each model. As the driving motivation for our work is *avoiding assumptions about OOD data*, we focus on baselines that do not rely on OOD data. Specifically, we employ the baselines **RbA** [41], **EAM** [22] and **M2A** [46] based on M2F and consider the general benchmarks **SML** [29] and **MM** as mask variants of **MSP** [27] on M2F. While **RbA** explicitly reports results for an OOD-free version, we use the OOD-free versions of **EAM** and **M2A** presented in the corresponding ablation studies of the works. Further, we use the prior-assumption-free U3HS [20], which is based on DeeplabV3+ [9]. All implementation details are provided in Appendix A.

In Fig. 3, we visualize the uncertainty scores predicted by different methods for two examples. While EAM, RbA, and M2A assign high uncertainties to parts of the animal in the bottom row only, P2F successfully identifies the anomalous animal objects in both rows. In Fig. 4, we present the results for SMIYC Road Anomaly, FS Static, and L&F obstacle track of FS in terms of the trade-off between AP and FPR they realize. P2F consistently balances the two metrics



Figure 5. P2F model prediction on Oodis [43]. Red boxes mark unseen instances. P2F effectively distinguished unknown anomalies even the ignored outside L&F region of interest.

Method	No		L&F		Anomaly		Obstacles		Mean	
	Aux. Models	OOD Data	AP $\uparrow$	AP50 $\uparrow$	AP $\uparrow$	AP50 $\uparrow$	AP $\uparrow$	AP50 $\uparrow$	AP $\uparrow$	AP50 $\uparrow$
UGainS [42]	✗	✗	27.14	45.82	11.42	19.15	27.22	46.54	25.19	42.81
M2A [46]	✓	✗	11.73	23.64	4.78	9.03	17.23	28.44	13.73	24.3
U3HS [20]	✓	✓	0.19	0.73	0	0	0.22	0.62	0.19	0.58
P2F [ours]	✓	✓	<b>5.60</b>	<b>14.55</b>	<b>0.59</b>	<b>1.25</b>	<b>2.25</b>	<b>6.88</b>	<b>3.21</b>	<b>8.85</b>

Table 1. Comparison of anomaly instance segmentation methods on the **official OoDIS[43] benchmark**, including the three subsets L&F, Road Anomaly and Road Obstacles. Best scores without additional requirements are in bold.

favorably while outperforming in both metrics for SMIYC Road Anomaly and FS. For L&F P2F is only marginally outperformed by EAM in terms of AP which significantly lacks in FPR compared to P2F. For SMIYC Road Anomaly, M2A only realizes a good AP at the cost of a very high FPR. These results underline the effectiveness of our uncertainty estimation in the context of anomaly segmentation. Since P2F detects instances we focus on the novel and more challenging anomaly **instance** segmentation task for further analysis.

**Anomaly Instance Segmentation:** We continue the evaluation by examining anomaly instance segmentation by submitting to the novel OoDIS benchmark [43]. OoDIS extends the previously used L&F [44], SMIYC [5] Road Anomaly, and Road Obstacles track by adding instance annotations allowing a more complex evaluation. Because of its small objects and misc class, we consider this task as the most challenging.

In Tab. 1, we report the results of the official OoDIS benchmark evaluation compared to other competitors listed on the benchmark’s official website. While M2A and UGainS show strong performances, they rely on OOD data knowledge and additional external models to specifically target the anomalies the benchmark encapsulates. Among models that do not rely on some sort of OOD data, P2F outperforms existing methods by a great margin. In Fig. 5, we visualize a prediction of P2F on an L&F sample of OoDIS. Besides excellent closed-world performance, P2F detects multiple anomalous obstacles, including the trash bins that are not part of the Cityscapes semantic classes on which the model was trained. Additionally, panoptic L&F results are shown in Appendix C. In Appendix B.4, we supply the results of the OoDIS benchmark on the publicly available

validation set comprising 100 L&F samples of the FS [3] split. In this setting, we again focus on U3HS [20] as it does not require assumptions about OOD data. Again, P2F shows high merits here.

**Open-World Segmentation:** The next task we evaluate is open-world panoptic segmentation. We defer an evaluation of semantic segmentation to Appendices B.1 and B.2. In the panoptic setting, individual instances must only be segmented according to their semantics but also distinguished from each other. The number of available baselines is limited, especially when requiring models to not rely on prior assumptions about OOD data, e.g. by explicitly training on a *void*-class. EOSPN [28] and DDOSP [62] target the panoptic setting but require void class supervision on parts of the unknown classes. U3HS [20] generalizes to all the tasks we evaluate and is the only other method without

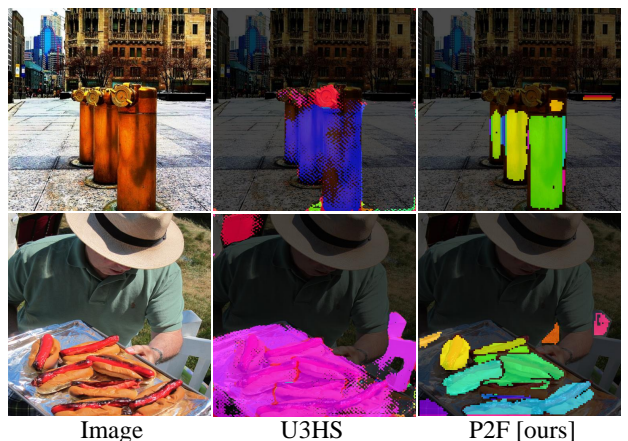


Figure 6. Comparison of anomaly instance segmentation on unseen instances on COCO [35].

Method	No void	Closed-World			unseen		
		PQ↑	SQ↑	RQ↑	PQ↑	SQ↑	RQ↑
EOPSN	✗	36.50	76.32	45.06	7.43	74.55	9.97
DDOPSN	✗	37.93	77.28	46.80	8.39	81.52	10.29
U3HS [20]	✓	22.03	69.03	27.92	9.62	72.84	13.20
P2F [ours]	✓	<b>41.34</b>	<b>78.60</b>	<b>50.79</b>	<b>10.71</b>	<b>79.96</b>	<b>13.39</b>

Table 2. Performance comparison on the COCO validation set [35] in closed- and open-world panoptic segmentation on full size.

Method	Closed-W.			Open-W.		
	PQ↑	SQ↑	RQ↑	PQ↑	SQ↑	RQ↑
U3HS [20]	46.53	78.87	58.99	41.21	79.77	51.67
P2F [ours]	<b>59.40</b>	<b>80.78</b>	<b>72.34</b>	<b>45.25</b>	<b>80.69</b>	<b>54.68</b>

Table 3. Closed and open-world evaluation on Cityscapes [14].

any OOD assumptions.

In Tab. 2, we evaluate P2F on COCO with the commonly used leave-out classes [20, 28, 62] preparation (see Appendix A). As evaluation metrics in open-world panoptic segmentation, we consider Panoptic Quality (PQ), Segmentation Quality (SQ), and Recognition Quality (RQ) scores for known and unseen classes, since EOPSN and DDOPSN require a part of the unknown classes for training. While EOPSN and DDOPSN leverage additional training void classes to predict left-out classes as void, the uncertainty-based approaches P2F and U3HS can eclipse both of them except for SQ. Nevertheless, our P2F outperforms U3HS in all three metrics, showcasing its performance.

In Fig. 6, we show visual results on COCO [35] for unseen classes of P2F and U3HS. For the top image, U3HS assigns the correct semantics but fails to separate individual instances. In contrast, P2F can distinguish between objects. For the bottom image, U3HS gets confused by the baking tray, while P2F manages to segment the individual unknown instances. In general, the P2F manages to extract more fine-grained structures compared to U3HS. Further results and visual examples are presented in Appendices B.2 and C.

Method	PQ↑	SQ↑	RQ↑
U3HS [20]	7.94	64.11	12.37
RbA* [41]	7.30	71.85	10.17
EAM* [22]	8.79	72.09	12.20
M2A* [46]	9.91	73.45	13.49
P2F [ours]	<b>11.22</b>	<b>74.47</b>	<b>15.06</b>

Table 4. Panoptic on unseen L&F in the setting of [20] after training on Cityscapes [14]. \* Uses our P2F postprocessing.

In Tab. 3, we report results on the Cityscapes open- and closed-world setting [20], where we investigate how much

Filter	Sym. Dice	Evid. Sampl.	Road Anomaly		FS L&F Obstacle	
			AP↑	FPR95↓	AP↑	FPR95↓
✗	✓	✓	40.5	46.4	66.4	<b>16.8</b>
✗	✗	✓	31.7	62.3	18.5	28.4
✓	✗	✓	53.1	72.7	45.3	95.9
✓	✓	✗	47.2	58.9	23.1	22.2
✓	✓	✓	<b>58.6</b>	<b>46.3</b>	<b>66.6</b>	<b>16.8</b>

Table 5. Ablation study of the main components of P2F.

the uncertainty thresholding influences the prediction in the absence of any anomalies. We further evaluate L&F in the setting as introduced by [20] in Tab. 4. For Cityscapes, P2F outperforms U3HS in all categories even though its performance decreases in non-closed-world settings. Especially for L&F, P2F significantly improves in PQ and RQ score, further experiments can be found in Appendix B.3.

**Ablation Study:** In Tab. 5, we study the influence of no-object mask filtering, the evidential sampling (II), and the symmetric dice loss (III). While the mask filter has only a minor influence on the FPR, the AP for Road Anomaly is negatively impacted by this ablation. Similarly, the symmetric dice loss mainly boosts the FPR, and evidential sampling increases the AP. Further ablations in Appendix B.5.

**Limitations:** Although P2F shows remarkable performance on a vast amount of tasks and benchmarks, the number of competing methods that do not rely on assumptions about OOD data is limited. By submitting P2F to the official OoDIS benchmark, we contribute a novel baseline that meets this requirement and, therefore, provides more reliable uncertainty in practice.

## 6. Conclusion

We introduce Prior2Former (P2F), the first evidential approach to mask-based vision transformers. P2F quantifies uncertainty by predicting the evidence of a Beta prior to the binary segmentation masks. This informs its embeddings to enable high-quality clustering of anomalous instances. P2F addresses several open-set segmentation tasks (anomaly segmentation, semantic and panoptic open-world segmentation, and anomaly instance segmentation) with one architecture and training procedure. Other than most prior work, it does not rely on assumptions about OOD data. This makes it highly applicable to real-world use cases where these assumptions are often unrealistic. Over an extensive experimental evaluation, we confirm the efficacy of P2F and its improvement over other OOD-free approaches. Especially in the recent OoDIS anomaly instance segmentation benchmark, P2F outperforms these competitors by a significant margin.



# Prior2Former - Evidential Modeling of Mask Transformers for Assumption-Free Open-World Panoptic Segmentation

## Supplementary Material

### A. Experimental Details

In this section, we provide details about the individual experimental setup and baselines, as well as the implementation details.

#### A.1. Anomaly Segmentation

For evaluating anomaly segmentation, we compare P2F against several baselines based on M2F [12] and U3HS [20] on the SMIYC [4] benchmark. The datasets used include SMIYC Road Anomaly [5], FS [3], and FS L&F [3]. All these benchmarks employ Cityscapes [14] as their in-distribution data source. The Cityscapes dataset consists of 19 classes — 8 categorized as "things" and 11 as "stuff" — captured from various cities across Germany. We employ the official SMIYC evaluation script with the addition of the FS dataset. Following the official evaluation, void-labeled regions are ignored for computing results for all three datasets. For FS L&F, only the region of interest, typically the road in front of the vehicle, is evaluated. The official metric requires an image-shaped array with anomaly scores and dynamically selects the best-fitting threshold per image. As *avoiding prior knowledge* is a fundamental aspect of our work, we primarily focus on metric-based baselines without OOD usage. Specifically, we employ the baselines **RbA** [41], **EAM** [22] and **M2A** [46] based on M2F and implemented the general benchmarks **SML** [29] and **MM** as mask variant of **MSP** [26] on M2F. While **RbA** reports an OOD-free version, we use the OOD-free versions of **EAM** and **M2A** presented in their ablation study. Further, we use the prior knowledge-free U3HS [20], which is based on DeeplabV3+ [9].

In contrast to how the respective papers evaluate these methods, EAM, RbA, and M2A are trained on the panoptic segmentation task, not on semantic segmentation. We use the same ResNet50 [24] backbone architecture for all methods to enable comparability between M2F-based approaches and U3HS. Additionally, EAM, RbA, and M2A train on OOD data to supervise anomaly detection. We omit this to mitigate assumptions about OOD data to enable a fair comparison of the uncertainty metric. Therefore, all presented M2F-based baselines are primarily post-processing functions applied to the output of a standard M2F model. For M2A, a global mask attention mechanism replaces the "local" mask attention during training.

For SML, we apply the maximum logit standardization to the logits  $L(x)$  of the M2F model introduced in Sec. 3:

$$L(x)_c = \sum_{i=1}^{N_m} p_i(c) \cdot m_i[h, w], \quad (13)$$

Let  $\mathbb{T}$  be the set over all training images and let  $L(x)_c \in \mathbb{R}^{H \times W}$  be the pixel-wise logits of class  $c$ . We compute the mean and standard deviation  $\mu, \sigma \in \mathbb{R}^K$  of these maximum logits over all classes:

$$\begin{aligned} \mu_c &= \text{MEAN}(\{L_{\hat{c}(x)}[h, w] \mid 1 \leq h \leq H, 1 \leq w \leq W, x \in \mathcal{X}_{\text{train}}\}) \end{aligned} \quad (14)$$

$$\begin{aligned} \sigma_c &= \text{STD}(\{L_{\hat{c}(x)}[h, w] \mid 1 \leq h \leq H, 1 \leq w \leq W, x \in \mathcal{X}_{\text{train}}\}) \end{aligned} \quad (15)$$

where

$$\hat{c}(x) = \arg \max_{c \in \{1, \dots, K\}} L_c(x)[h, w].$$

Hence,

$$U^{\text{SML}}[h, w] = -\frac{L_{\hat{c}}[h, w] - \mu_{\hat{c}}}{\sigma_{\hat{c}}}.$$

To obtain the SML uncertainty  $U^{\text{SML}}[h, w]$  for a pixel at position  $h, w$  of image  $x$ , we standardize the maximum logit  $L_{\hat{c}}^{(x)}[h, w]$  using the mean and standard deviation computed from all pixels  $[h, w]$  over all images  $x$  in the training set, where the class  $\hat{c}$  has the greatest logit.

The Maximum Mask (MM) baseline presents a mask-based variant of MSP [26]:

$$U^{\text{MM}}[h, w] = -\max_{i \in \{1, \dots, N_m\}} m_i[h, w].$$

For MSP [26], the maximum softmax probability of the current pixel is taken as the confidence score, whereas for MM, the maximum sigmoid probability over all masks serves as the confidence score. The uncertainty estimates according to EAM [22], RbA [41], and M2A [46] follow the corre-

sponding papers:

$$U^{(\text{EAM})}[h, w] = - \sum_{i=1}^{N_m} m_i[h, w] \cdot \left( \max_{c=1, \dots, K} (p_i(c)) \right), \quad (18)$$

$$U^{(\text{RBA})}[h, w] = - \sum_{c=1}^K \text{sigmoid}(L_c[h, w]), \quad (19)$$

$$U^{(\text{M2A})}[h, w] = \left( 1 - \max_{c=1, \dots, K} L_c[h, w] \right) \cdot R_M[h, w], \quad (20)$$

where the sigmoid function is applied elements-wise and  $R_M$  is the mask filter as presented in M2A [46], such that the uncertainty  $U^{(\text{M2A})}[h, w]$  is set to zero if there is no mask for pixel  $[h, w]$  where the masks score  $m_i[h, w] > 0.5$  and the predicted class is "road" or a "thing" class and the softmax confidence is greater than 0.95. We evaluate M2A by only using the pixel-wise filter  $m_i[h, w] > 0.5$  since all other models do not include class-specific information for the detection of anomalies. Note that for the M2A uncertainty, the logits are obtained from a model trained with global mask attention.

Since the SMIYC metric expects one anomaly score per pixel on a given image, the logical "and" between thresholded distances and anomaly scores, as implemented by U3HS [20], can not be used for the evaluation metric. Hence, for U3HS, the Dirichlet strength from the semantic head is used as an anomaly score.

## A.2. Anomaly Instance Segmentation

The task of Anomaly Instance Segmentation is evaluated using the official OoDIS benchmark code [43]. This benchmark assesses performance on three datasets: an unknown split of L&F [44], as well as the test splits of the SMIYC RoadAnomaly21 [5] and RoadObstacles21 [5]. The evaluation requires binary images containing the recognized anomalies and a confidence score for each binary image. An anomaly instance prediction with an Intersection over Union (IoU) greater than 0.5 and the highest confidence score is considered a positive prediction contributing to the true positive and false positive rates. All other predictions, not counted as valid predictions for another anomaly, are considered false positives.

For submission and evaluation on the publicly available validation set containing only L&F [44] data, P2F and U3HS [20] are trained on the Cityscapes dataset.

## A.3. Closed-World and Open-World Panoptic Segmentation

Here, we detail the experimental setup for computing the PQ and mIoU metrics on the two datasets COCO [35] and BDD100k [64] for P2F and U3HS [20].

**COCO:** For the COCO [35] dataset, we preprocess the data by excluding all images containing any of the 20% least frequent classes in the training set, specifically: *baseball bat, bear, fire hydrant, frisbee, hairdryer, hot dog, keyboard, microwave, mouse, parking meter, refrigerator, scissors, snowboard, stop sign, toaster, and toothbrush*, which aligns with [20, 62]. The images in the validation set containing any held-out classes are placed into a separate set, termed the open-world validation set, while the remaining images form the closed-world validation set. The semantic labels of the known classes are retained, while the semantic labels of the held-out classes are merged into a single OOD class. We then evaluate the mIoU and PQ of the open-world validation set, treating all anomalies as belonging to the OOD class. We use COCO panopticapi<sup>1</sup> and torchmetrics<sup>2</sup> for PQ and mIoU evaluation, respectively. Following the training scheme presented in M2F [46] for COCO, we employ a random resize crop augmentation strategy during training, which maintains the aspect ratio of the input images. During validation, we maintain the original size of the COCO images. This approach differs from the scheme used in U3HS, where images are resized for both training and evaluation.

**BDD100k:** For the BDD100k [64] dataset, we follow the evaluation and training procedure employed for COCO. For the dataset split, we use the proposed class settings of BDD anomaly [27] and leave out the classes motorcycle and bicycle. In contrast to [27], we use the panoptic labels instead of the semantic labels to enable a panoptic evaluation. Note that besides the instance information, the panoptic labels additionally have an increased number of classes compared to the semantic labels. We construct the closed-world training and validation sets and the open-world validation set similarly but evaluate all scores based on the respective torchmetrics implementation. We restrict the evaluation of mIoU and PQ only on instances that cover more than 2,500 pixels. This is because the depth values in the dataset show significant variability, resulting in many small anomalies that cover only a few pixels. Including these small anomalies in the evaluation does not meaningfully contribute to understanding the models' ability to recognize the held-out classes.

**Cityscapes:** For open and world segmentation, we followed the setup described by [20] and used the standard training setup as suggested of M2F for all M2F-based baselines, including P2F. For U3HS we used the setup described in their paper and used the respective evaluation settings. For the Lost & Found evaluation, we used a resized version as done by [20] and a full-size version to maintain a fair evaluation.

<sup>1</sup><https://github.com/COCODataset/panopticapi>

<sup>2</sup><https://lightning.ai/docs/torchmetrics/stable/>

#### A.4. Implementation Details

We train P2F and M2F on **Cityscapes** using a series of augmentations. Specifically, we apply a random zoom crop with a crop size of (1024, 512) and a zoom range of (1.0, 2.0). Additionally, we utilize a color jitter augmentation with a brightness delta of 32, a hue delta of 18, contrast adjustments in the range of (0.5, 1.5), and saturation changes within (0.5, 1.5). We also include a random horizontal flip with a probability of 0.5. The color jittering is necessary because we use the models trained on Cityscapes for evaluation on SMIYC and Oodis. Without this augmentation, different lighting conditions, especially of the sky, could result in high anomaly scores.

We train the models with a batch size of 16, a learning rate of 0.0001, and a learning rate of 0.00001 for the backbone, using the AdamW optimizer [38] with a weight decay of 0.05. A polynomial learning rate scheduler with a power of 0.9 is employed. Gradients are clipped at 0.01 according to the L2 norm. The training is conducted for 450 epochs, which corresponds to approximately 90,000 iterations. Hence, we follow the training as suggested for M2F [12] on Cityscapes, with the only difference of adding the color jittering for the more robust uncertainty estimation.

For the **COCO** dataset, we employ a random zoom crop that keeps the aspect ratio fixed with a zoom range of (0.1, 2.0) and a crop size of (512, 512). No color jittering is used. The optimizer and scheduler configurations, random horizontal flip, and gradient clipping remain the same, but the batch size is increased to 32, and the training is performed over 50 epochs. In summary, we use a training scheme closely matching the M2F [12] configuration for COCO. However, we changed the crop size from (1024, 1024) to (512, 512) and the batch size from 16 to 32 for known settings, which improved the convergence speed. For the the unseen class setup, we maintained the (1024, 1024) setup.

For the **BDD** dataset, M2F [12] does not provide a configuration. Hence, we primarily follow the training on Cityscapes as a related dataset. We scale the images within the range of (1.0, 2.0) and cropped both dimensions by half to a size of (640, 360), similar to the cropping applied in Cityscapes. No color jittering is used. All other parameters are consistent with those used for Cityscapes.

Across **all** datasets, we train using a no-object loss coefficient of 0.1, a class loss weight  $\lambda_{cls} = 2.0$ , a symmetric dice loss weight  $\lambda_{sDice} = 5.0$ , and an evidential loss weight  $\lambda_{evi} = 0.1$  for P2F. The evidential loss weight is tuned to ensure that the loss values of the symmetric dice and evidential loss have similar absolute values. We use 200 object queries for both the baselines and P2F, which is necessary to generate a sufficient number of valid mask predictions on the SMIYC Road Anomaly and SMIYC Road Obstacle datasets. All other hyperparameters for model building

and training remain consistent with those used in the official M2F repository<sup>3</sup>.

For **postprocessing** the predictions of P2F, we set the object-mask-threshold to 0.5, compared to 0.8 in the original M2F model. This threshold on the mask prediction probability determines if an object is present in the panoptic prediction. However, since the beta prior predictions of P2F are more restrictive, we choose a lower threshold value.

To create the anomaly instance segmentation, we introduce a threshold  $t$  to the uncertainty estimates of P2F. The corresponding feature vectors of the pixel embedding  $F_E$  are then clustered using DBSCAN [17] with parameters eps and min-samples. The mask correspondence is determined using a scalar product between the predicted mask features and the pixel embedding. Hence, it is natural to use one minus the cosine similarity instead of an Euclidean distance for the DBSCAN, as it is the normalized scalar product of the two vectors. For the submission on OoDIS, the uncertainty threshold  $t$  is set to 2 times the standard deviation away from the mean uncertainty on the training set  $t = -0.6$  for the L&F split. The overall uncertainty on SMIYC Road Anomaly and SMIYC Road Obstacle is greater since the images cover uncommon scenarios and conditions. Hence, we increase the threshold to 3.5 times the standard deviation, i.e.,  $t = -0.4$ . For COCO and BDD, we follow the same approach of determining the threshold and, therefore, set  $t = -0.6$ . The parameter eps strongly influences the granularity of the clustering algorithms. Evaluating the embedding space, we use 0.04 in all experiments. Except for COCO, we set eps = 0.02 due to the wider variety of semantic classes and instances. The min-samples parameter is set to 17, however, clustering the embedding is robust against changes in this parameter, with values ranging from 10 to 23 being effective.

## B. Additional Experiments

Besides the experiments provided in Sec. 5, we report additional experiments on closed-world segmentation, open-world semantics segmentation, the OoDIS validation set, as well as a further ablation study of our uncertainty metric.

### B.1. Closed World Segmentation

To compare P2F in closed-world segmentation, we compare it to the vanilla M2F and a naive Dirichlet Prior network (DPN) [39] for M2F for Cityscapes. We follow the training settings provided in [12] and use the Cityscapes [14] script for evaluation. Besides the mIoU, we also report the category-wise IoU (cIoU). In Tab. 6, it can be seen that P2F performs similarly to M2F. This contrasts with the massive performance drop of the DPN head.

<sup>3</sup><https://github.com/facebookresearch/Mask2Former>

Model	mIoU $\uparrow$	cIoU $\uparrow$	PQ $\uparrow$	SQ $\uparrow$	RQ $\uparrow$
M2F	77.3	90.2	60.29	81.28	73.15
M2F DPN	64.5	88.4	50.29	67.20	61.70
P2F [ours]	<b>77.0</b>	<b>89.1</b>	<b>59.41</b>	<b>80.74</b>	<b>72.34</b>

Table 6. Comparison of M2F with different evidential heads on Cityscapes on Panoptic Segmentation. Best evidential heads are marked in bold.

Method	BDD Anomaly		COCO	
	Closed	Open	Closed	Open
U3HS [20]	29.16	16.32	33.19	22.77
P2F [ours]	<b>35.73</b>	<b>29.12</b>	<b>46.00</b>	<b>33.56</b>

Table 7. Open- and closed-world semantic segmentation comparison using mIoU metric for BDD Anomaly on COCO.

Method	Closed-W.			Open-W.		
	PQ $\uparrow$	SQ $\uparrow$	RQ $\uparrow$	PQ $\uparrow$	SQ $\uparrow$	RQ $\uparrow$
U3HS [20]	<b>36.82</b>	80.93	16.32	17.81	75.59	23.63
P2F [ours]	32.67	<b>81.68</b>	<b>29.0</b>	<b>29.10</b>	<b>79.43</b>	<b>36.66</b>

Table 8. Closed and open-world evaluation on the BDD100k anomaly dataset [64].

## B.2. Open-World and Closed-World Segmentation

Besides the results reported on panoptic segmentation in Sec. 5, we study open- and closed-world semantic segmentation. In Tab. 7, we show the mIoU results for BDD100k [64] anomaly and COCO [35] with the left-out classes listed in Appendix A.3. Like in panoptic segmentation, P2F ranks the highest in all settings. In the non-panoptic setting, ContMAV [55] has shown promising results but also relies on void supervision during training. Furthermore, we find that the available official implementation<sup>4</sup> does not permit stable training (as flagged by other users as well).

In Tab. 8 we report the panoptic quality metric of U3HS and P2F on BDD100k [64] anomaly dataset. U3HS shows a strong closed-world performance in PQ and RQ. However, P2F achieves the highest scores in the open-world setting as well as for SQ in the closed-world setting.

## B.3. Further Experiments on L&F

To further compare using the setting of unseen L&F data as introduced by [20], we compare the reduced size evaluation with the baselines reported by [20] and an M2F confidence uncertainty. It can be seen, that the additional baselines struggle with this task. The confidence baseline of M2F shows a surprisingly strong performance.

<sup>4</sup><https://github.com/PRBonn/ContMAV>

Method	Assumptions	PQ $\uparrow$	SQ $\uparrow$	RQ $\uparrow$
EOPSN [28]	data, void	0*	0*	0*
OSIS [59]	data, void	1.45	65.11	2.23
U3HS [20]	none	7.94	64.24	12.37
M2A* [46]	none	9.91	73.45	13.49
M2F*	none	9.02	<b>75.34</b>	11.98
P2F [ours]	none	<b>11.22</b>	74.47	<b>15.06</b>

Table 9. Results on the Lost&Found (unseen) dataset with the settings of [20]. [28] and [59], are taken from [20]. \* Uses our postprocessing.

In addition, to the setting reported by [20], we report the performance of P2F in comparison to other masked-based uncertainty methods in Tab. 10 using the full resolution of the L&F dataset. We train M2A without OOD data. We further report M2F using a classical confidence measure as uncertainty, which diverges for this task. We also report the uncertainty measures of RbA [41] and EAM [22]. These results show that all these methods profit heavily from the increased resolution, nevertheless P2F maintains the highest scores for PQ and RQ.

Method	PQ $\uparrow$	SQ $\uparrow$	RQ $\uparrow$
M2A* [46]	21.06	<b>73.14</b>	28.79
M2F*	0.00	0.00	0.00
EAM* [22]	18.39	71.35	25.78
RbA* [41]	15.54	70.65	21.99
P2F [ours]	<b>22.07</b>	69.54	<b>31.73</b>

Table 10. Unseen L&F performance metrics on full-size resolution. \* Uses our postprocessing.

## B.4. OoDIS Validation Set

In addition to the official OoDIS [43] benchmark scores, we present results on the validation set of OoDIS comprising 100 L&F [44] instance anomaly labels. We report the scores for the OOD-free and extra-model-free U3HS and P2F in Tab. 11. For U3HS, we experimented with 4 different uncertainty thresholds and reported the best. The results of both models are slightly better compared to the benchmark evaluation on a larger L&F, while their ranking remains unchanged.

Backbone	Model	No Aux. Models		No OOD Data	
				AP $\uparrow$	AP50 $\uparrow$
R50	U3HS [20]	✓	✓	0.61	2.04
R50	P2F [ours]	✓	✓	<b>8.17</b>	<b>16.13</b>

Table 11. Comparison of different Anomaly Segmentation Methods on the validation set of OoDIS.



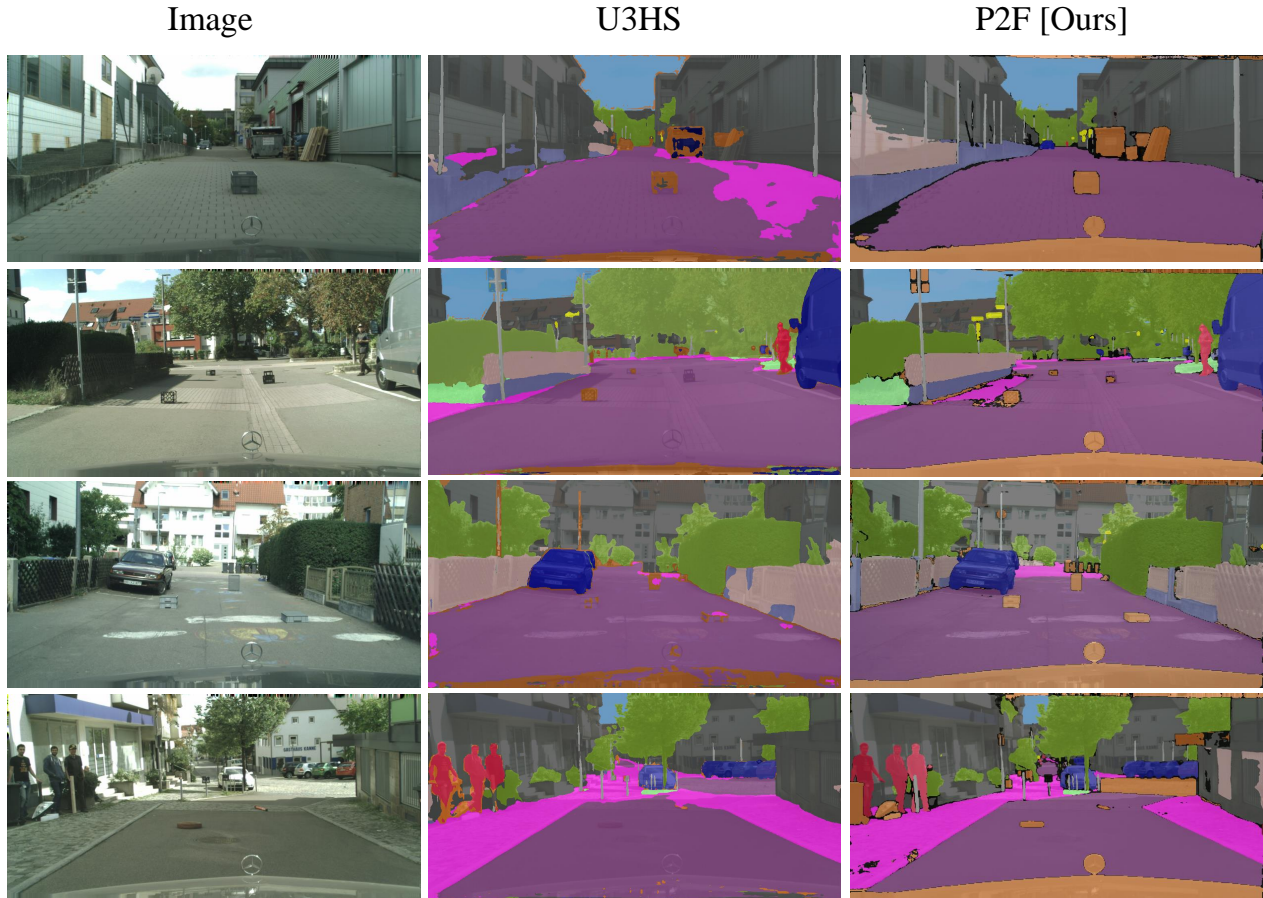


Figure 7. Open-World panoptic segmentation on L&F test set after training on Cityscapes [14].

### B.5. Uncertainty Ablation Study

In this section, we conduct further ablation studies in addition to the reported study in Sec. 5. In Tab. 12, we compare the predictive uncertainty suggested by M2F [12] with the uncertainty of P2F. It can be seen that the P2F uncertainty is more effective on AP for the Road Anomaly split of SMIYC and provides a major improvement in the FPR of both datasets. This underlines the benefit of the evidential mask selection in our uncertainty. Overall our P2F shows strong uncertainty statistics. Nevertheless, for minor semantics shifts like L&F, the mask filtering seems to be less important.

### C. Additional Qualitative Assessment:

In Fig. 7 we show visual results of open-world panoptic segmentation on the L&F test set. Anomaly predictions are marked in brown. For all predictions including the anomaly prediction, different shades mark distinct instances. The L&F dataset includes the obstacles on the road as anomalies, but also other objects that have not been trained on dur-

Method	Road Anomaly		FS L&F Obstacle	
	AP $\uparrow$	TPR95 $\downarrow$	AP $\uparrow$	TPR95 $\downarrow$
Prediction Uncertainty	48.6	62.2	61.2	88.4
P2F uncertainty [ours]	<b>58.6</b>	<b>46.3</b>	<b>66.6</b>	<b>16.8</b>

Table 12. Uncertainty comparison of P2F using the classical prediction uncertainty and P2F uncertainty definition.

ing training on Cityscapes. These include trashcans, pipes, the back side of traffic signs, and pallets. For anomaly detection, U3HS uses a double threshold strategy where both the classification uncertainty and distances in the embedding are thresholded. For anomaly detection, both predictions need to surpass the individual thresholds. This can lead to not detecting anomalies as in the second and third row of Fig. 7, but also results in less noise in the prediction. Further, the L&F features uncommon textures of the street, which results in confusion between sidewalk and road or wrongly detected anomalies, as visible in row one for U3HS



Figure 8. Visual comparison of anomaly instance segmentation on held-out classes on BDD [64]. The high diversity and unbalanced class distribution seem to confuse the DPN-based U3HS [20]. Nonetheless, U3HS showed a strong segmentation quality for the rare classes like the traffic sign poles. P2F, managed to detect the unknown motorcycle or bicycles more precisely, given its less class imbalance affected Beta’s prior approach.



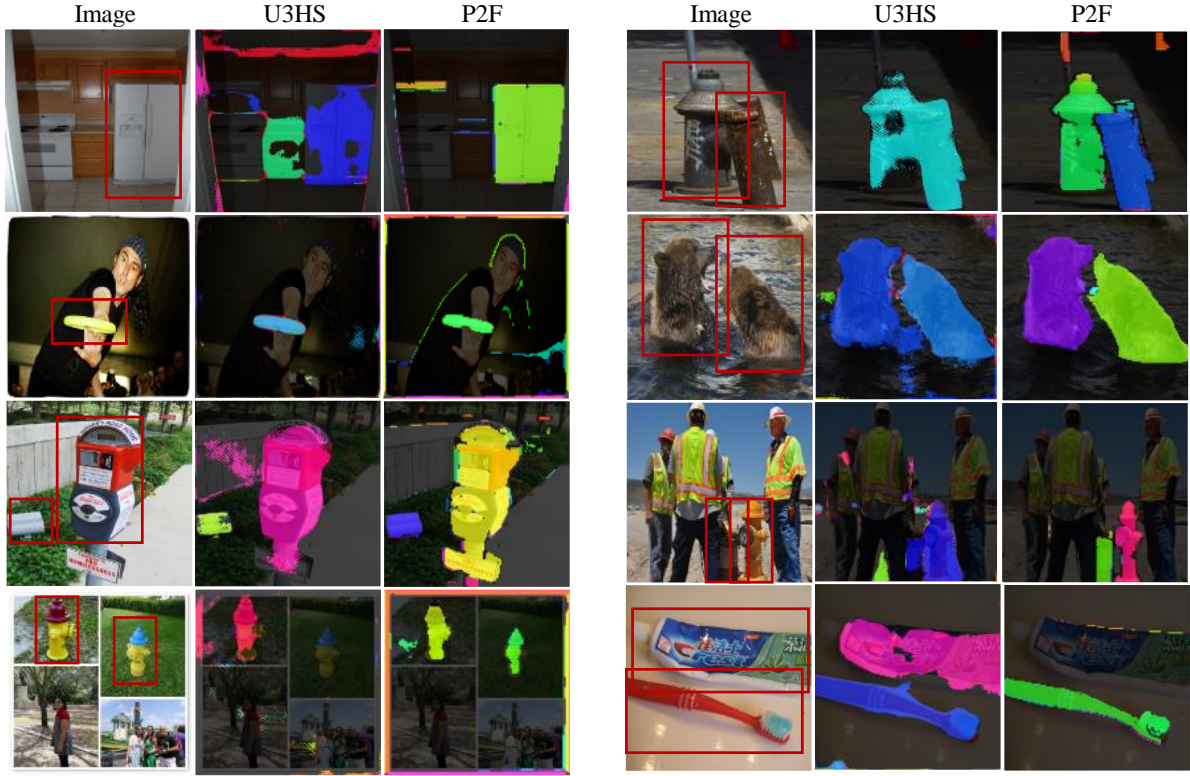


Figure 9. Visual comparison of anomaly instance segmentation on held-out classes on COCO [35]. It can be seen that U3HS shows a strong performance for individual and larger objects but can get confused with related objects, like different kitchen objects in the top left. Additionally, it suppresses the combined uncertainty and distance approach uncertainty at the object border. P2F provides with the direct mask supervision and Beta prior a more robust separation of different instances, while improving the segmentation quality.

and in rows two and four for P2F.

We also provide further visual results of P2F and U3HS [20] on the BDD [64] dataset in Fig. 8 and on the COCO [35] Dataset in Fig. 9. Compared to Cityscapes, the BDD dataset comprises a higher variety of classes and different scenarios, making the anomaly instance segmentation task more challenging. This is demonstrated by the increased false positive rate of both models. Nonetheless, they are able to detect anomalies reasonably well in this challenging environment. However, the much smaller embedding dimension of U3HS has difficulties in identifying unseen instances, which results in cluttered predictions. This can be seen, for example, in rows one and three in Fig. 8. While the explicit regularization of the embeddings prevents uncertainty between instances, P2F might predict uncertainties between the transition or regions. Improve the uncertainty instance clustering to reject these remains future work. Additionally, given the high-class imbalance of the dataset, U3HS tends to confuse rare classes with anomalies, for example, the traffic sign pole in row three. In contrast, P2F clearly detects the anomaly as its embeddings are high dimensional and because of its additional mask supervision

signal. Additionally, U3HS also marks the rider of the bicycles and motorcycles as an anomaly, whereas P2F separates well-visible humans, which is a natural phenomenon since human beings are present in the training set.

In comparison to BDD [64], the COCO [35] dataset features less cluttered images but includes a greater variety of classes. The total number of objects per image is lower, and the objects themselves are generally larger. In this setup, U3HS [64] and P2F perform well on simple images with only one anomaly as well as on more difficult images with several objects and anomaly instances. The distance thresholding of U3HS [20] and uncertainty thresholding suppresses uncertainty estimates at the edge of two classes. The pure uncertainty thresholding of P2F marks them as an anomaly, as visible in row 2 in Fig. 9. P2F consistently shows a superior object segmentation as well as instance separation compared to U3HS [20]. This underlines the effectiveness of our proposed Beta prior and the high quality of the embedding space learned by P2F.

## References

- [1] Jan Ackermann, Christos Sakaridis, and Fisher Yu. Maskomaly: zero-shot mask anomaly segmentation. In *BMVC*, 2023. 3
- [2] Joost Van Amersfoort, Lewis Smith, Yee Whye Teh, and Yarin Gal. Uncertainty estimation using a single deep deterministic neural network. *International Conference on Machine Learning*, 2020. 2
- [3] Hermann Blum, Paul Edouard Sarlin, Juan Nieto, Roland Siegwart, and Cesar Cadena. The fishyscapes benchmark: Measuring blind spots in semantic segmentation. *International Journal of Computer Vision*, pages 3119–3135, 2021. 2, 6, 7, 9
- [4] Robin Chan, Krzysztof Lis, Svenja Uhlemeyer, Hermann Blum, Sina Honari, Roland Siegwart, Pascal Fua, Mathieu Salzmann, and Matthias Rottmann. Segmentmeifyoucan: A benchmark for anomaly segmentation. In *Neurips Datasets and Benchmarks Track*, 2021. 9
- [5] Robin Chan, Matthias Rottmann, and Hanno Gottschalk. Entropy maximization and meta classification for out-of-distribution detection in semantic segmentation. In *ICCV*, 2021. 2, 6, 7, 9, 10
- [6] Bertrand Charpentier, Daniel Zügner, and Stephan Günnemann. Posterior network: Uncertainty estimation without ood samples via density-based pseudo-counts. In *NeurIPS*, 2020. 2
- [7] Bertrand Charpentier, Oliver Borchert, Daniel Zügner, Simon Geisler, and Stephan Günnemann. Natural posterior network: Deep bayesian uncertainty for exponential family distributions. In *ICML*, 2022. 2
- [8] Liang-Chieh Chen, George Papandreou, Florian Schroff, and Hartwig Adam. Rethinking atrous convolution for semantic image segmentation. *arXiv*, 1706.05587, 2017. 2
- [9] Liang-Chieh Chen, Yukun Zhu, George Papandreou, Florian Schroff, and Hartwig Adam. Encoder-decoder with atrous separable convolution for semantic image segmentation. In *Proceedings of the European Conference on Computer Vision (ECCV)*, 2018. 2, 6, 9
- [10] Bowen Cheng, Maxwell D Collins, Yukun Zhu, Ting Liu, Thomas S Huang, Hartwig Adam, and Liang-Chieh Chen. Panoptic-deeplab: A simple, strong, and fast baseline for bottom-up panoptic segmentation. In *CVPR*, 2020. 1, 2
- [11] Bowen Cheng, Alexander G. Schwing, and Alexander Kirillov. Per-pixel classification is not all you need for semantic segmentation. In *Neurips*, 2021. 2, 3
- [12] Bowen Cheng, Ishan Misra, Alexander G. Schwing, Alexander Kirillov, and Rohit Girdhar. Masked-attention mask transformer for universal image segmentation. In *CVPR*, 2022. 1, 2, 3, 5, 9, 11, 13
- [13] Hyunjun Choi, Hawook Jeong, and Jin Young Choi. Balanced energy regularization loss for out-of-distribution detection. In *CVPR*, 2023. 3
- [14] Marius Cordts, Mohamed Omran, Sebastian Ramos, Timo Rehfeld, Markus Enzweiler, Rodrigo Benenson, Uwe Franke, Stefan Roth, Bernt Schiele, Daimler Ag R&d, and T U Darmstadt. The cityscapes dataset for semantic urban scene understanding. In *Proceedings of the IEEE Conference on Computer Vision and Pattern Recognition (CVPR)*, 2016. 1, 8, 9, 11, 13
- [15] Anja Delić, Matej Grcić, and Siniša Šegvić. Outlier detection by ensembling uncertainty with negative objectness. *Arxiv*, 2402.15374, 2024. 2, 3
- [16] Arthur P Dempster. A generalization of bayesian inference. *Journal of the Royal Statistical Society: Series B (Methodological)*, 30(2):205–232, 1968. 3
- [17] Martin Ester, Hans-Peter Kriegel, Jörg Sander, and Xiaowei Xu. A density-based algorithm for discovering clusters in large spatial databases with noise. In *Proceedings of the Second International Conference on Knowledge Discovery and Data Mining*, page 226–231. AAAI Press, 1996. 6, 11
- [18] Yarin Gal and Zoubin Ghahramani. Dropout as a bayesian approximation: Representing model uncertainty in deep learning. In *Proceedings of the International Conference on Machine Learning (ICML)*, 2016. 2
- [19] Stefano Gasperini, Jan Haug, Mohammad-Ali Nikouei Mahani, Alvaro Marcos-Ramiro, Nassir Navab, Benjamin Busam, and Federico Tombari. Certainnet: Sampling-free uncertainty estimation for object detection. *IEEE Robotics and Automation Letters*, 7(2):698–705, 2022. 2
- [20] Stefano Gasperini, Alvaro Marcos-Ramiro, Michael Schmidt, Nassir Navab, Benjamin Busam, and Federico Tombari. Segmenting known objects and unseen unknowns without prior knowledge. In *ICCV*, 2023. 1, 2, 3, 6, 7, 8, 9, 10, 12, 14, 15
- [21] Jakob Gawlikowski, Cedrique Rovile Njiteucheu Tassi, Mohsin Ali, Jongseok Lee, Matthias Humt, Jianxiang Feng, Anna Kruspe, Rudolph Triebel, Peter Jung, Ribana Roscher, Muhammad Shahzad, Wen Yang, Richard Bamler, and Xiao Xiang Zhu. A survey of uncertainty in deep neural networks. *Arxiv*, 2107.03342, 2021. 2
- [22] Matej Grcić, Josip Šarić, and Siniša Šegvić. On advantages of mask-level recognition for outlier-aware segmentation. In *CVPR Workshops*, 2023. 3, 6, 8, 9, 12
- [23] Chuan Guo, Geoff Pleiss, Yu Sun, and Kilian Q Weinberger. On calibration of modern neural networks. In *International conference on machine learning*, pages 1321–1330. PMLR, 2017. 3
- [24] Kaiming He, Xiangyu Zhang, Shaoqing Ren, and Jian Sun. Deep residual learning for image recognition. In *Proceedings of the IEEE/CVF Conference on Computer Vision and Pattern Recognition (CVPR)*, 2016. 6, 9
- [25] Matthias Hein, Maksym Andriushchenko, and Julian Bitterwolf. Why relu networks yield high-confidence predictions far away from the training data and how to mitigate the problem. In *Proceedings of the IEEE/CVF conference on computer vision and pattern recognition (CVPR)*, 2019. 3
- [26] Dan Hendrycks and Kevin Gimpel. A baseline for detecting misclassified and out-of-distribution examples in neural networks. In *ICLR*, 2017. 3, 9
- [27] Dan Hendrycks, Steven Basart, Mantas Mazeika, Andy Zou, Joe Kwon, Mohammadreza Mostajabi, Jacob Steinhardt, and Dawn Song. Scaling out-of-distribution detection for real-world settings. In *ICML*, 2022. 6, 10



- [28] Jaedong Hwang, Seoung Wug Oh, Joon-Young Lee, and Bohyung Han. Exemplar-based open-set panoptic segmentation network. In *CVPR*, 2021. 1, 2, 3, 7, 8, 12
- [29] Sanghun Jung, Jungsoo Lee, Daehoon Gwak, Sungha Choi, and Jaegul Choo. Standardized max logits: A simple yet effective approach for identifying unexpected road obstacles in urban-scene segmentation. In *ICCV*, 2021. 3, 6, 9
- [30] Alex Kendall and Yarin Gal. What uncertainties do we need in bayesian deep learning for computer vision? *Advances in neural information processing systems*, 30, 2017. 3
- [31] Alexander Kirillov, Kaiming He, Ross Girshick, Carsten Rother, and Piotr Dollár. Panoptic segmentation. In *CVPR*, 2019. 2
- [32] Alexander Kirillov, Eric Mintun, Nikhila Ravi, Hanzi Mao, Chloe Rolland, Laura Gustafson, Tete Xiao, Spencer Whitehead, Alexander C Berg, Wan-Yen Lo, Piotr Dollár, and Ross Girshick. Segment anything. In *ICCV*, 2023. 2
- [33] Balaji Lakshminarayanan, Alexander Pritzel, and Charles Blundell Deepmind. Simple and scalable predictive uncertainty estimation using deep ensembles. In *Neurips*, 2017. 2
- [34] Chen Liang, Wenguan Wang, Jiaxu Miao, and Yi Yang. Gmmseg: Gaussian mixture based generative semantic segmentation models. In *Neurips*, 2022. 2
- [35] Tsung-Yi Lin, Michael Maire, Serge Belongie, James Hays, Pietro Perona, Deva Ramanan, Piotr Dollár, and C Lawrence Zitnick. Microsoft coco: Common objects in context. In *ECCV*, 2014. 7, 8, 10, 12, 15
- [36] Jeremiah Zhe Liu, Zi Lin, Google Research, Shreyas Padhy, Dustin Tran, Tania Bedrax-Weiss, and Balaji Lakshminarayanan. Simple and principled uncertainty estimation with deterministic deep learning via distance awareness. In *Neurips*, 2020. 2
- [37] Weitang Liu, Xiaoyun Wang, John D Owens, and Yixuan Li. Energy-based out-of-distribution detection. In *Neurips*, 2020. 3
- [38] Ilya Loshchilov and Frank Hutter. Decoupled weight decay regularization. In *ICLR*, 2019. 11
- [39] Andrey Malinin and Mark Gales. Predictive uncertainty estimation via prior networks. In *NeurIPS*, 2018. 2, 11
- [40] Jishnu Mukhoti, Andreas Kirsch, Joost Van Amersfoort, Philip H S Torr, and Yarin Gal. Deep deterministic uncertainty: A new simple baseline. In *CVPR*, 2023. 2, 4
- [41] Nazir Nayal, Misra Yavuz, João F. Henriques, and Fatma Güney. Rba: Segmenting unknown regions rejected by all. In *ICCV*, 2022. 3, 6, 8, 9, 12
- [42] Alexey Nekrasov, Alexander Hermans, Lars Kuhnert, and Bastian Leibe. Ugains: Uncertainty guided anomaly instance segmentation. In *GCPR*, 2023. 1, 2, 7
- [43] Alexey Nekrasov, Rui Zhou, Miriam Ackermann, Alexander Hermans, Bastian Leibe, and Matthias Rottmann. Oodis: Anomaly instance segmentation benchmark. *Arxiv*, 2406.11835, 2024. 2, 7, 10, 12
- [44] Peter Pinggera, Sebastian Ramos, Stefan Gehrig, Uwe Franke, Carsten Rother, and Rudolf Mester. Lost and found: Detecting small road hazards for self-driving vehicles. In *IROS*. IEEE, 2016. 1, 2, 6, 7, 10, 12
- [45] Alec Radford, Jong Wook Kim, Chris Hallacy, Aditya Ramesh, Gabriel Goh, Sandhini Agarwal, Girish Sastry, Amanda Askell, Pamela Mishkin, Jack Clark, et al. Learning transferable visual models from natural language supervision. In *International conference on machine learning*, pages 8748–8763. PMLR, 2021. 1
- [46] Shyam Nandan Rai, Fabio Cermelli, Dario Fontanel, Carlo Masone, and Barbara Caputo. Unmasking anomalies in road-scene segmentation. In *ICCV*, 2023. 3, 6, 7, 8, 9, 10, 12
- [47] Olaf Ronneberger, Philipp Fischer, and Thomas Brox. U-net: Convolutional networks for biomedical image segmentation. In *Medical Image Computing and Computer-Assisted Intervention (MICCAI)*, pages 234–241. Springer Verlag, 2015. 2
- [48] Yusuf Sale, Viktor Bengs, Michele Caprio, and Eyke Hüllermeier. Second-order uncertainty quantification: A distance-based approach. In *Forty-first International Conference on Machine Learning*, 2023. 4
- [49] Sebastian Schmidt and Stephan Günnemann. Stream-based active learning by exploiting temporal properties in perception with temporal predicted loss. In *Proceedings of the British Machine Vision Conference (BMVC)*, 2023. 2
- [50] Sebastian Schmidt, Qing Rao, Julian Tatsch, and Alois Knoll. Advanced active learning strategies for object detection. In *Proceedings of the IEEE Intelligent Vehicles Symposium (IV)*, 2020. 2
- [51] Sebastian Schmidt, Leonard Schenk, Leonard Schwinn, and Stephan Günnemann. A unified approach towards active learning and out-of-distribution detection. *arXiv*, 2405.11337, 2024. 2
- [52] Sebastian Schmidt, Ludwig Stumpp, Diego Valverde, and Stephan Günnemann. Deep sensor fusion with constraint safety bounds for high precision localization. In *2024 IEEE/RSJ International Conference on Intelligent Robots and Systems (IROS)*, pages 12256–12262. IEEE, 2024. 1
- [53] Sebastian Schmidt, Leonard Schenk, Leo Schwinn, and Stephan Günnemann. Joint out-of-distribution filtering and data discovery active learning. In *Proceedings of the IEEE/CVF Conference on Computer Vision and Pattern Recognition (CVPR)*, 2025. 2
- [54] Murat Sensoy, Lance Kaplan, and Melih Kandemir. Evidential deep learning to quantify classification uncertainty. In *Neurips*, 2018. 2, 3
- [55] Matteo Sodano, Federico Magistri, Lucas Nunes, Jens Behley, and Cyrill Stachniss. Open-world semantic segmentation including class similarity. In *CVPR*, 2024. 2, 3, 12
- [56] Maximilian Stadler, Bertrand Charpentier, Simon Geisler, Daniel Zügner, and Stephan Günnemann. Graph posterior network: Bayesian predictive uncertainty for node classification. In *Conference on Neural Information Processing Systems (NeurIPS)*, 2021. 2
- [57] Carole H. Sudre, Wenqi Li, Tom Vercauteren, Sebastien Ourselin, and M. Jorge Cardoso. Generalised dice overlap as a deep learning loss function for highly unbalanced segmentations. In *Deep Learning in Medical Image Analysis and Multimodal Learning for Clinical Decision Support*, pages 240–248, 2017. 3

- [58] Yu Tian, Yuyuan Liu, Guansong Pang, Fengbei Liu, Yuanhong Chen, and Gustavo Carneiro. Pixel-wise energy-biased abstention learning for anomaly segmentation on complex urban driving scenes. In *ECCV*, 2022. [3](#)
- [59] Kelvin Wong, Shenlong Wang, Mengye Ren, Ming Liang, and Raquel Urtasun. Identifying unknown instances for autonomous driving. In *Proceedings of the Conference on Robot Learning*, pages 384–393. PMLR, 2020. [12](#)
- [60] C. Zach X. Liu, Y. Lochman. GEN: Pushing the Limits of Softmax-Based Out-of-Distribution Detection. In *Proceedings of the IEEE/CVF Conference on Computer Vision and Pattern Recognition (CVPR)*, 2023. [2](#)
- [61] Enze Xie, Wenhai Wang, Zhiding Yu, Anima Anandkumar, Jose M Alvarez, and Ping Luo. Segformer: Simple and efficient design for semantic segmentation with transformers. In *Neurips*, 2021. [2](#), [3](#)
- [62] Hai-Ming Xu, Hao Chen, Lingqiao Liu, and Yufei Yin. Dual decision improves open-set panoptic segmentation. In *BMVC*, 2022. [1](#), [2](#), [3](#), [7](#), [8](#), [10](#)
- [63] Jingkan Yang, Pengyun Wang, Dejian Zou, Zitang Zhou, Kunyuan Ding, Wenxuan Peng, Haoqi Wang, Guangyao Chen, Bo Li, Yiyu Sun, Xuefeng Du, Kaiyang Zhou, Wayne Zhang, Dan Hendrycks, Yixuan Li, and Ziwei Liu. Openood: Benchmarking generalized out-of-distribution detection. In *Thirty-sixth Conference on Neural Information Processing Systems Datasets and Benchmarks Track*, 2022. [2](#)
- [64] Fisher Yu, Haofeng Chen, Xin Wang, Wenqi Xian, Yingying Chen, Fangchen Liu, Vashisht Madhavan, and Trevor Darrell. Bdd100k: A diverse driving dataset for heterogeneous multitask learning. In *CVPR*, 2020. [10](#), [12](#), [14](#), [15](#)
- [65] Hao Zhang, Fang Li, Lu Qi, Ming-Hsuan Yang, and Narendra Ahuja. Csl: Class-agnostic structure-constrained learning for segmentation including the unseen. In *AAAI Technical Track on Computer Vision VI*, 2023. [2](#)